J. Fluid Mech. (1991), *vol.* 225, *pp.* 395–422
Printed in Great Britain

An investigation of transition to turbulence in bounded oscillatory Stokes flows
Part 1. Experiments

By R. AKHAVAN[1,2], R. D. KAMM[2] AND A. H. SHAPIRO[2]

[1] Department of Mechanical Engineering, The University of Michigan, Ann Arbor, MI 48109-2125, USA

[2] Department of Mechanical Engineering, Massachusetts Institute of Technology, Cambridge, MA 02139, USA

(Received 11 September 1989 and in revised form 26 September 1990)

Experimental results on flow-field statistics are presented for turbulent oscillatory flow in a circular pipe for the range of Reynolds numbers $Re^{\delta} = U_0 \delta/\nu$ ($U_0 =$ amplitude of cross-sectional mean velocity, $\delta = (2\nu/\omega)^{\frac{1}{2}}$) = Stokes layer thickness) from 550 to 2000 and Stokes parameters $\Lambda = R/\delta$ ($R =$ radius of the pipe) from 5 to 10. Axial and radial velocity components were measured simultaneously using a two-colour laser-Doppler anemometer, providing information on ensemble-averaged velocity profiles as well as various turbulence statistics for different phases during the cycle. In all flows studied, turbulence appeared explosively towards the end of the acceleration phase of the cycle and was sustained throughout the deceleration phase. During the turbulent portion of the cycle, production of turbulence was restricted to the wall region of the pipe and was the result of turbulent bursts. The statistics of the resulting turbulent flow showed a great deal of similarity to results for steady turbulent pipe flows; in particular the three-layer description of the flow consisting of a viscous sublayer, a logarithmic layer (with von Kármán constant = 0.4) and an outer wake could be identified at each phase if the corresponding ensemble-averaged wall-friction velocities were used for normalization. Consideration of similarity laws for these flows reveals that the existence of a logarithmic layer is a dimensional necessity whenever at least two of the scales R, u_*/ω and ν/u_* are widely separated; with the exact structure of the flow being dependent upon the parameters $u_*/R\omega$ and $u_*^2/\omega\nu$. During the initial part of the acceleration phase, production of turbulence as well as turbulent Reynolds stresses were reduced to very low levels and the velocity profiles were in agreement with laminar theory. Nevertheless, the fluctuations retained a small but finite energy. In Part 2 of this paper, the major features observed in these experiments are used as a guideline, in conjunction with direct numerical simulations of the 'perturbed' Navier–Stokes equations for oscillatory flow in a channel, to identify the nature of the instability that is most likely to be responsible for transition in this class of flows.

1. Introduction

Oscillatory wall-bounded flows emerge in a variety of engineering applications in fields ranging from offshore engineering to biomedical sciences. An understanding of the dynamics and mechanisms of transition to turbulence in these flows is, therefore, of great practical interest. Many new and interesting questions arise, concerning not only the laminar–turbulent transition process but also regarding the effects of the imposed oscillations on the bursting events and turbulence production mechanisms in these wall flows. Nevertheless, relatively few studies have been reported in the literature on the subject.

In this study we restrict our discussion to oscillatory flows with zero time mean. For studies on periodic turbulent flows with non-zero time mean the reader is referred to the works of Mizushina, Maruyama & Shiozaki (1973), Mizushina, Maruyama & Hirasawa (1975). Ramaprian & Tu (1983), Tu & Ramaprian (1983) and Tardu, Binder & Blackwelder (1987).

Many of the earlier studies on oscillatory flows with zero time mean (Sergeev 1966; Merkli & Thomann 1975; Hino, Sawamoto & Takasu 1976; Ohmi *et al.* 1982), were directed towards defining the boundaries between the laminar and turbulent flow regimes. Four broad types of flows in the (Re^{δ}–Λ) space have been identified: (I) laminar flow; (II) disturbed laminar flow, where 'small-amplitude' perturbations appear superimposed on the velocity traces during the acceleration phase of the cycle but where otherwise the velocity traces agree with laminar theory; (III) intermittently turbulent flow, where turbulent bursts appear violently and explosively during the deceleration phase of the cycle while during the acceleration phase the flow reverts to laminar; and possibly (IV) fully turbulent flow, where the flow remains turbulent throughout the cycle. Flows of type (IV) have not actually been observed by any of the investigators, although it has been observed that, as Re^{δ} increases, flows of type (III) remain turbulent for increasingly larger portions of the cycle.

It is generally agreed that transition to flows of type (III) is a local event and is governed by the Reynolds number based on the Stokes boundary-layer thickness, as long as the boundary-layer thickness is small compared to the physical dimensions of the problem. For flows of liquids in pipes and channels with $\Lambda > 2$, a transitional Re^{δ} (independent of Λ) in the range of 500–550 has been reported by a number of investigators (Sergeev 1966; Hino *et al.* 1976; Ohmi *et al.* 1982). A similar value of $Re^{\delta}_{\text{crit}} \sim 565$ has also been reported by Li (1954) for transition in flow about an oscillating plate in an infinite medium. There have, however, been other reports specifying different values for the transitional Reynolds number. For example, Merkli & Thomann (1975) observed transition at $Re^{\delta}_{\text{crit}} \sim 280$ for flow in a pipe with air as the working fluid. In giving this value, Merkli & Thomann do not specify whether transition to flows of type (II) or of type (III) was intended. This lower value of $Re^{\delta}_{\text{crit}}$ is in good agreement with the results of Ohmi *et al.* for transition to flows of type (II), and falls within the range of Re^{δ} for which Hino *et al.* (1976) observed transition to flows of type (II). It differs from the results reported by Hino and coworkers in that in Hino's experiments the critical Re^{δ} for transition to flows of type (II) was dependent on Λ. In general, transition to flows of type (II) seems to be quite sensitive to the particular experimental set-up, whereas transition to flows of type (III) is very well defined and rather independent of the particular experimental set-up.

A theoretical explanation of the instability mechanism leading to transition to flows of either type (II) or type (III) has so far been unavailable, the major problem being the lack of a critical Reynolds number based on linear theories from which nonlinear theories could be developed. It is generally agreed that transition is due to the local instability of the Stokes boundary layers near the walls, and therefore much of the existing theoretical work addresses the stability of the basic Stokes layer. Theoretical work has so far been restricted to the study of infinitesimal disturbances for which the equations of motion can be linearized. Two classes of linear theories have been suggested; ones based on the assumption of quasi-steadiness, and those which take into account the time variation of the base flow but which can only predict the behaviour of the disturbances in the periodic steady state.

In quasi-steady theories (Collins 1963; Obremski & Morkovin 1969; Cowley 1987; Monkewitz & Bunster 1987), the time variation of the base velocity profile is neglected in the stability analysis and a series of 'frozen' profiles for different phases during the cycle are individually examined for stability. This approach is justified because the (convective) timescale for the growth or decay of the (inflexional) instabilities of the Stokes layer is much shorter than the (viscous) time variation of the base flow. Since a variety of base velocity profiles exist throughout a cycle, one would expect that during certain portions of the cycle the flow may be less stable than during others. This may seem encouraging in view of experimental observation of intermittently turbulent flows, until one realizes that a stability analysis of this kind predicts the most dangerous profiles to occur at the start of the acceleration phase of the cycle, in direct conflict with experimental observations which show that turbulent bursts appear violently with the start of the deceleration phase. This type of instability, however, may explain transition to flows of type (II) as will be discussed in more detail in Part 2 of this paper (Akhavan, Kamm & Shapiro 1991).

In time-dependent solutions (von Kerczek & Davis 1974; Hall 1978), an extension of the Floquet Theorem is used to provide a description of the behaviour of the disturbances in the periodic steady state. Using this approach von Kerczek & Davis (1974) studied the stability of a 'finite' Stokes layer (consisting of an oscillatory plate with a second stationary plate located a distance of $\Lambda\delta$ away) but found the flow to be stable for all the Reynolds numbers and disturbance wavenumbers, α, considered ($0 < Re^{\delta} < 800$, $\Lambda = 8$, $0.3 < \alpha < 1.3$). Furthermore, they found no evidence of transient growth of disturbances during a portion of the cycle such that the disturbances may grow to finite amplitudes within one cycle. Hall (1978) presented a different version of this theory in which there was no need for an upper boundary, but he too found that the flow was stable for all Reynolds numbers considered. In the case of the infinite Stokes layer, the least stable eigenmodes were associated with a continuous spectrum of eigenvalues located outside the layer. Since the 'finite' layer only has a discrete spectrum of eigenvalues, Hall warns us against inferring the behaviour of the infinite layer from 'finite' models. So far no convincing explanation has been given of how these time-dependent calculations relate to quasi-steady theories.

In the present work we wish to bridge some of the gap between theory and experiment by attempting to identify an instability mechanism that would result in flow-field statistics similar to those that have been observed experimentally. The problem is approached in two directions. On the one hand, experimental results are provided on the major features of transitional and turbulent oscillatory flows such as the transitional Reynolds number, timescales of the instability and various flow-field statistics. On the other hand, direct numerical simulations of the Navier–Stokes equations using spectral techniques are used to follow the evolution of the flow once it has been subjected to various classes of infinitesimal or finite-amplitude, two- or three-dimensional disturbances. The class of disturbances that is most successful in predicting features in agreement with experiments is identified.

An earlier experimental study of turbulence statistics in purely oscillatory channel flows has been reported by Hino *et al.* (1983) for the case $Re^{\delta} = 876$, $\Lambda = 12.8$. The present studies generally confirm those results and extend them to a broader range

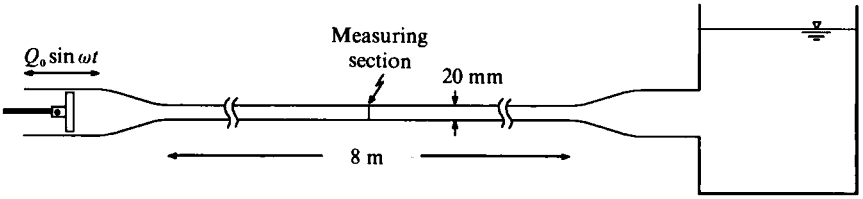

FIGURE 1. Schematic of the apparatus.

of the Re^{δ}–A space. Moreover, we present certain features that are more pronounced in the present experiments and which were not elaborated by Hino *et al.*

2. Experimental apparatus and data analysis

Experiments were conducted in a quartz circular pipe, 2 cm in inner diameter and 8 m long (figure 1). The length of the pipe was chosen such that under all flow conditions the pipe length was at least three times the stroke length of the flow; thereby ensuring that the flow in the middle portion of the pipe was not suffering from any end effects. The pipe was connected through bell-shaped transitions to a piston-cylinder at one end, and a wide-area head tank at the other.

An electrohydraulic servovalve (MOOG model 76-102) with feedback control on the velocity and input command from a function generator was used to drive the piston. The quality of the sinusoidal motion generated by this mechanism was checked by monitoring the motion of the piston with a velocity transducer (LVDT, Schaevitz model 6L3-VTZ) and also by computing the flow rates based on laser-Doppler anemometer (LDA) measurements of velocity profiles. In each case a fast Fourier transform (FFT) fit was performed to check the purity of the sinusoidal motion. Except for a small 'glitch' that occurred at flow reversal, the resulting motions could be fitted closely with a pure sine wave.

Velocities were measured with a DISA two-colour LDA, in which the blue (488 nm) and green (514 nm) lines of an Argon laser (Lexel) were used to measure simultaneously the axial and radial velocity components. The LDA was equipped with a Bragg cell and was operated in the backscatter mode. Counters were used for signal processing. The probe volume had dimensions of 20 x 20 x 100 μm and fringes were 2 μm apart. The front lens in the LDA system was mounted on a two-axis linear translation stage with micrometer control of position to within 0.0001 in. This traversing mechanism was used to position the probe volume at selected points along a diameter within the quartz pipe.

The optical distortion due to the curvature of the surfaces of the quartz pipe was eliminated by using, for the working fluid, an aqueous solution of ammonium thiocyanate with the same index of refraction as that of quartz ($n_d = 1.458$). The solution was mixed until the correct index of refraction was achieved (approximately equal weights of ammonium thiocyanate salt and distilled water). A hand-held refractometer (Extech, model K502192) with 0–90% sucrose range ($n_d =$ 1.333–1,512) and $\pm 2\%$ accuracy was used to measure the index of refraction of the solution. Otherwise, the solution was Newtonian and had properties very similar to those of water ($\rho = 1.1$ g/cm^3, $\nu = 1.32$ cS). Optical distortion due to the curvature of the outer surface of the pipe was also eliminated in a similar manner by immersing the pipe, at the measurement site, in a rectangular chamber with flat quartz windows that was filled with the same index-matched fluid.

A variety of seeding particles including alumina, latex, silicon carbide and titanium dioxide were examined. Titanium dioxide (with particles of diameter from 0.5 to 1 μm) was chosen over the others because of its good signal-to-noise ratio in the backscatter mode and ability to follow the smaller scales of turbulent motion.

The Doppler information was recorded on a MINC PDP11/23 data acquisition computer. The LDA counters could communicate with this computer via a direct memory access parallel interface board (DRV11-J), and were wired to interrupt the computer every time a Doppler burst was verified by both counters (within 15 μs of each other). Because the base flow was time dependent, the time of arrival of each Doppler burst in relation to the periodic motion of the flow had to be determined. This was achieved by making use of the computer's internal clock. This clock was reset at the beginning of each cycle (at a point corresponding to zero positive-going flow rate into the system) and was programmed to count the time in fractions of 1/240th of the period of oscillation. Upon arrival of each Doppler burst, the register containing this time was read and the time information was stored together with the Doppler data. In addition, the instantaneous pressure drop through the quartz pipe (measured with a Microswitch pressure transducer) and the velocity of the driving piston (as measured by the LVDT velocity transducer) were sampled through the computer's A/D converters at a rate of 240 times per cycle and the information was stored and later transferred to a VAX 11/750 minicomputer for further processing.

Typically, on the order of 2000 Doppler bursts per second were processed in this manner. The rate-limiting factor was the amount of seeding that could be used before the flow became opaque. Sampling was continued until at least 100 data points had been recorded for each of the 240 fractions of the cycle.

3. Experimental results

3.1. *Laminar flow regime*

To check the reliability of our experimental methods, the velocity profiles for an example of laminar flow with an imposed flow rate $Q = Q_0 \sin \omega t$ ($Re^{\delta} = 233$, $\Lambda = 3.6$) were measured and compared to the theoretical solutions of Womersley (1955) and Uchida (1956). The results are shown in figures 2 and 3. Figure 2 is a plot of the phase variation of the axial velocity at various radial locations. The solid lines represent the theory. At each radial location the axial velocity changes sinusoidally with time. The points near the wall have a phase lead with respect to the core. Both of these features are captured accurately in the experiments. In figure 3, the experimental velocity profiles at selected phases during the cycle are compared to theory. The agreement between theory and experiment is in general very good.

3.2. *Turbulent flow regime*

In the turbulent flow regime we have made detailed measurements for three different flow conditions; $\Lambda = 10.6$ with $Re^{\delta} = 1080$ and 1720; and $\Lambda = 5.7$ with $Re^{\delta} = 957$. All these flows are of type (III). The characteristics of the resulting turbulent flow will first be discussed in detail for the flow condition corresponding to $\Lambda = 10.6$, $Re^{\delta} = 1080$. Most of the features demonstrated by this flow are common to all the cases studied and as such this data point may be considered as a prototype flow. The effect of variation of Re^{δ} and Λ will then be discussed.

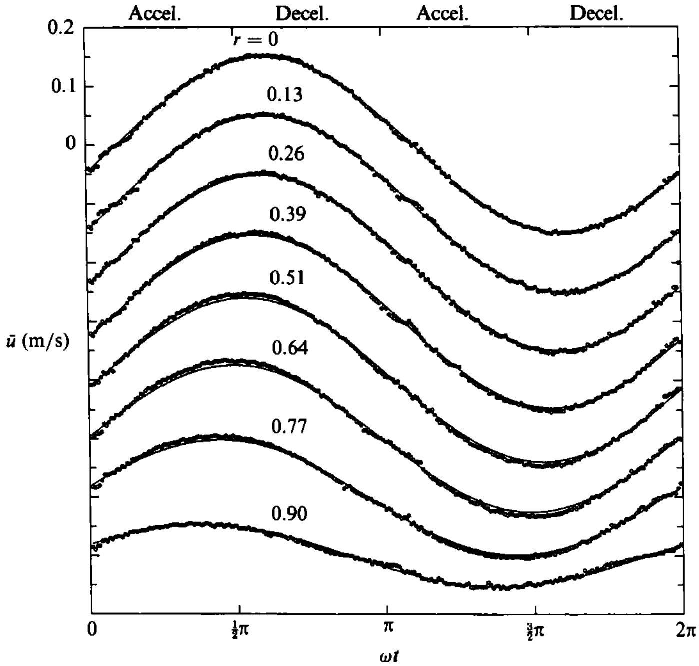

FIGURE 2. Phase variation of axial velocity in the laminar flow regime from experiments (symbols) compared to laminar theory (solid lines). ($R^\delta = 233$, $\Lambda = 3.6$.)

3.2.1. *Mean velocity distributions*

Ensemble-averaged velocities are defined as

$$\bar{u}(r, \omega t) = \frac{1}{N}\sum_{j=1}^{N} u_j(r, \omega t + 2\pi(j-1)), \tag{1}$$

where N is typically 100 and phase of the cycle is resolved to 1/240th of the period of oscillation.

The temporal variation of the ensemble-averaged axial velocity at various radial locations is plotted in figure 4 for turbulent flow at $\Lambda = 10.6$, $Re^\delta = 1080$. The solid lines represent the laminar solutions under the same flow rate and are plotted for reference.

During the turbulent portion of the cycle ($5\pi/12 < \omega t < \pi$, $17\pi/12 < \omega t < 2\pi$), as a result of turbulent bursts, there is significant momentum exchange between the low-speed fluid near the wall and the high-speed fluid nearer the centre of the pipe. This momentum exchange is rather dramatically seen in figure 4 as a hump during the deceleration phase for $0.9 < r/R < 1.0$ ($0.0 < y < \delta$; y = distance from the wall) and a simultaneous dip for $0.6 < r/R < 0.9$ ($\delta < y < 4\delta$). Outside this active layer, in the region $0 < r/R < 0.6$ ($4\delta < y < R$) is an inviscid outer 'core', where the velocity varies in phase with the imposed flow in a nearly sinusoidal manner. The hump at the beginning of the deceleration phase near the centre of the pipe ($0 < r/R < 0.3$) is due to a turbulent 'wake' at the centre of the pipe, as will be discussed shortly.

From these data one can construct, as in figure 5, profiles of ensemble-averaged axial velocity for different phases during the cycle. In this figure the solid lines drawn through the data points are best fits to the data calculated by a binomial smoothing

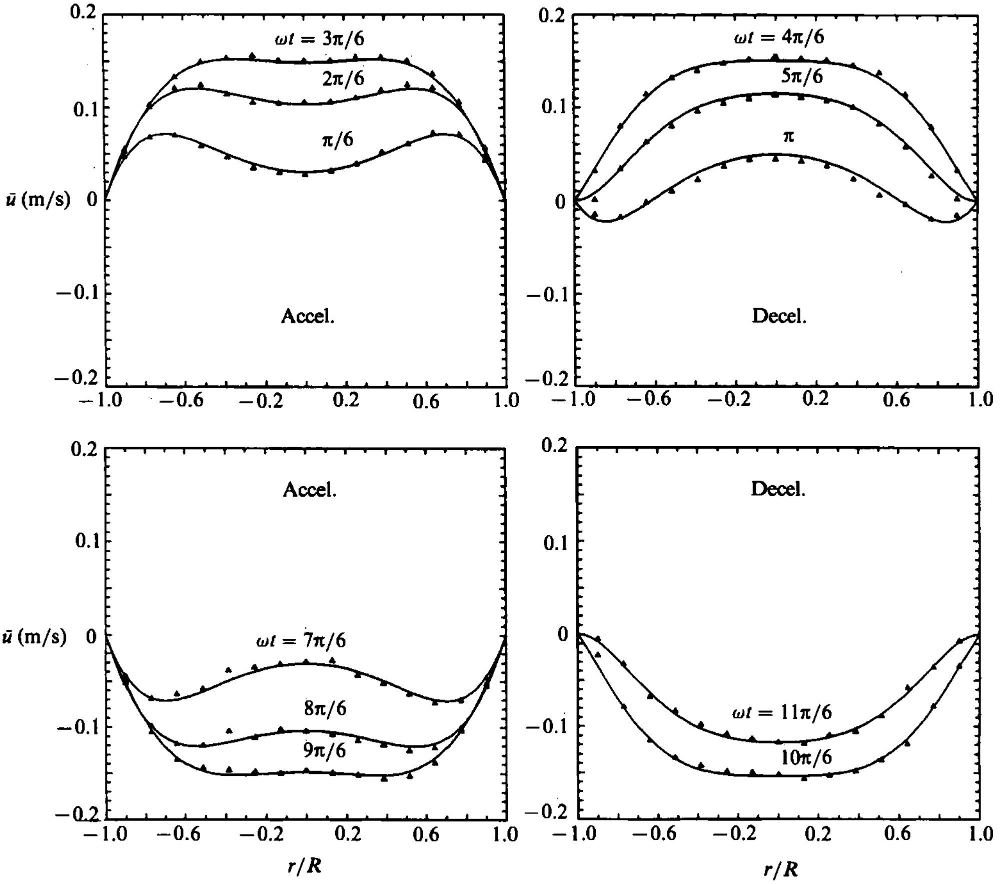

FIGURE 3. Comparison between experimental velocity profiles in the laminar flow regime ($Re^{\delta} = 233$, $\Lambda = 3.6$) and laminar theory.

algorithm (Marchand & Marmet 1983), while the 'bare' solid lines represent the laminar solution under the same flow rate. These profiles reveal a marked difference between the structure of the flow during the acceleration phase as compared to the deceleration phase.

During the acceleration phase of the cycle ($0 < \omega t < \frac{1}{2}\pi$, $\pi < \omega t < \frac{3}{2}\pi$), the wall shear stresses (slopes of the velocity profiles at the wall) agree well with laminar theory. Nevertheless, during this phase, the ensemble-averaged velocity profiles depart dramatically from the solutions of Womerseley (1955) and Uchida (1956) outside the wall region. The solutions of Womersely and Uchida, of course, refer to laminar flow in the 'periodic steady state' and are characterized by large phase differences between the motion of the boundary layers and the core. In the present problem, however, laminar flow during the acceleration phase is followed by turbulent flow during the deceleration phase. Large Reynolds stresses during the deceleration phase transfer momentum radially so efficiently that any phase differences between the motion of the boundary and the core are eliminated. At the end of the deceleration phase, when the integrated flow is zero, the velocity profile is also virtually uniform (and zero) across the cross-section. The laminar flow in the acceleration phase that follows then behaves not according to the solutions of Womersley and Uchida, but as in the problem of start-up from rest of sinusoidal laminar flow in a pipe. We have

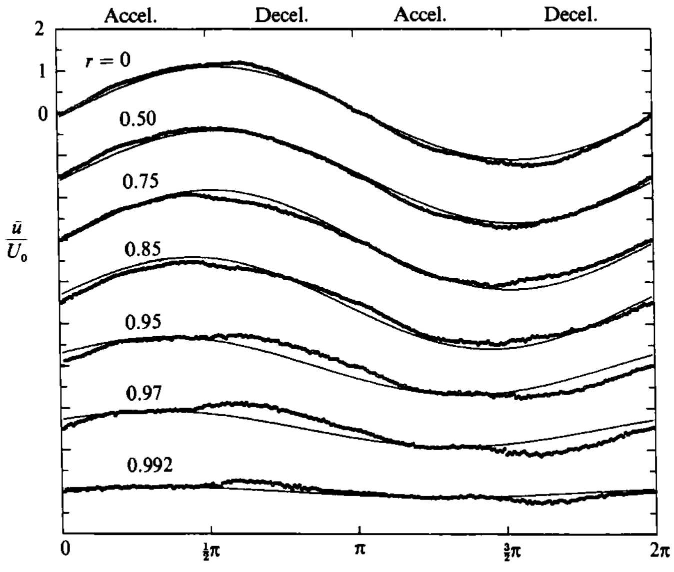

FIGURE 4. Phase variation of the ensemble-averaged axial velocity in the turbulent flow regime (symbols) compared to laminar theory. ($Re^{\delta} = 1080$, $\Lambda = 10.6$.)

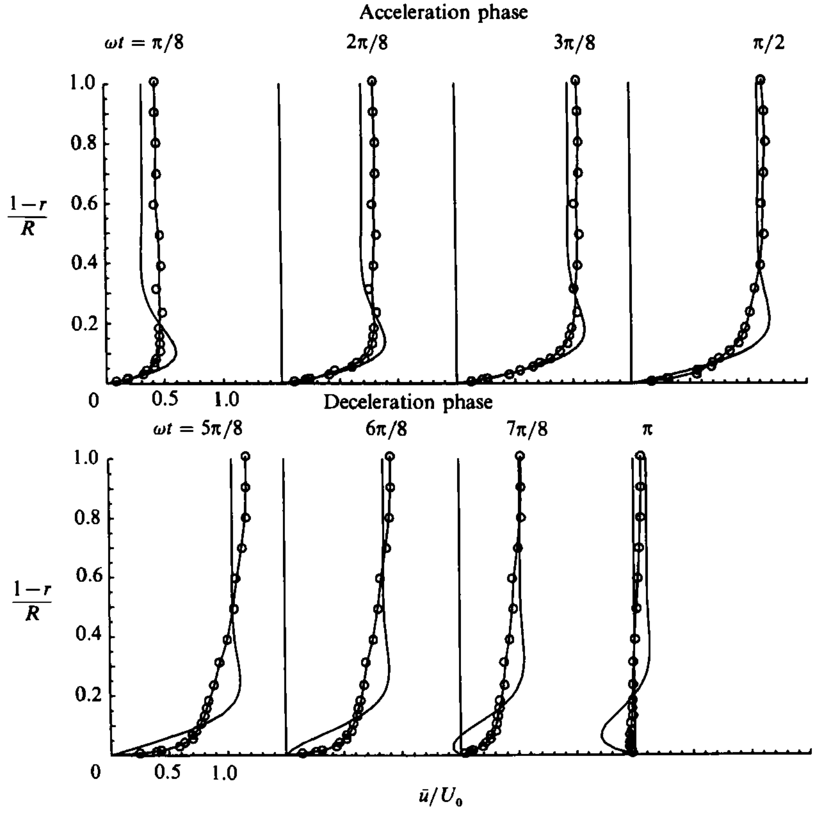

FIGURE 5. Ensemble-averaged axial velocity profiles in the turbulent flow regime (—O—) compared to laminar profiles. ($Re^{\delta} = 1080$, $\Lambda = 10.6$.)

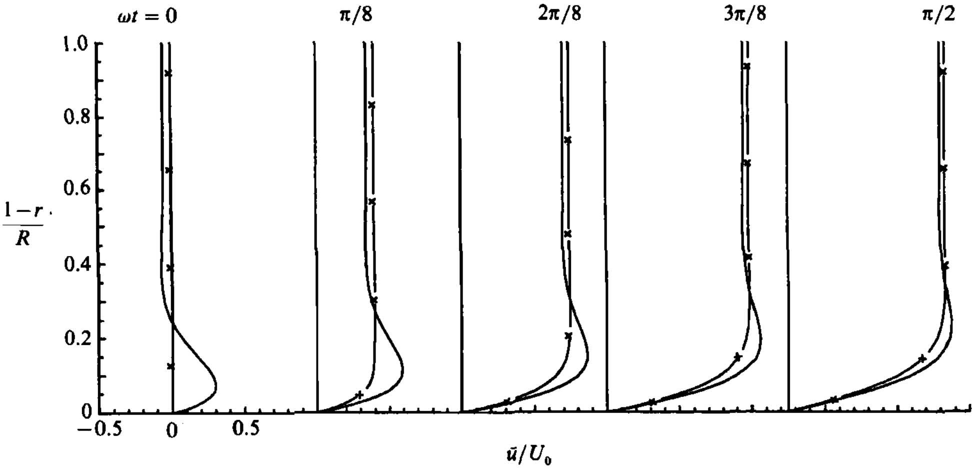

FIGURE 6. Velocity profiles for start-up from rest of laminar flow in a channel (—×—) compared to Womersley's solution ($\Lambda = 10$).

numerically integrated the Navier–Stokes equations to find these profiles, with the results shown in figure 6. The results agree well with the measured data during the early part of the acceleration phase.

In contrast, the profiles during the deceleration phase exhibit boundary layers that are considerably thinner than those for laminar flow. The detailed structure of the flow during this period is best seen in semi-logarithmic plots of velocity as a function of the distance from the wall and will be discussed shortly. For now note the characteristic concavity of these profiles in the region just outside the wall layer at $y/R \sim 0.2$, which is characteristic of turbulent boundary layers in adverse pressure gradients. Note also that the profiles at the end of the deceleration phase ($\omega t = \pi$ or 2π), at zero flow rate, show practically no phase differences between the motion of the boundary layer and the core. As mentioned earlier, this is due to efficient momentum exchange by turbulent Reynolds stresses.

3.2.2. *Wall-friction velocity*

The wall-friction velocity, $u_* \equiv (\tau_w/\rho)^{\frac{1}{2}}$ is a measure of the wall shear stress τ_w. In fully developed pipe flow, the ensemble-averaged pressure gradient, $\partial\bar{p}/\partial x$, is independent of the axial and radial directions and the overall momentum balance in the axial direction may be written as

$$\frac{\tau_w}{\rho} = u_*^2 = \tfrac{1}{2}R\left(-\frac{1}{\rho}\frac{\partial\bar{p}}{\partial x} - \frac{\partial\bar{u}_{av}}{\partial t}\right), \tag{2}$$

where
$$\bar{u}_{av}(\omega t) = \frac{2}{R^2}\int_0^R \bar{u}(r,\omega t)\, r\, \mathrm{d}r = U_0 \sin\omega t.$$

Ensemble-averaged values of $u_*^2(\omega t)$ were calculated from (2), using experimental measurements of $\partial\bar{p}/\partial x$ made with a differential pressure transducer and $\bar{u}_{av}(\omega t)$ calculated from LDA measurements of velocity. Figure 7 shows $u_*^2(\omega t)$ as so determined for the case $Re^\delta = 1080$, $\Lambda = 10.6$. Values of τ_w/ρ are positive for $0 < \omega t < \pi$, and negative for $\pi < \omega t < 2\pi$. This change in sign is merely a reflection of the reversal of the direction of flow for $\pi < \omega t < 2\pi$.

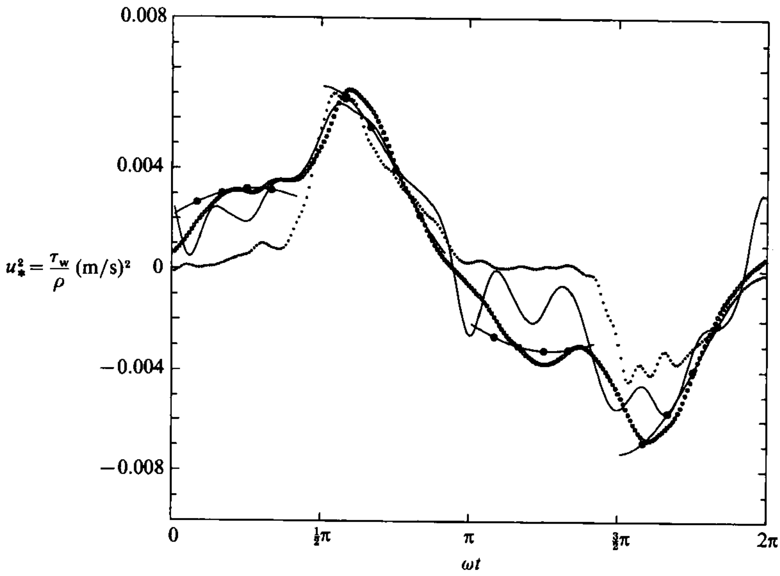

FIGURE 7. Phase variation of the wall-friction velocity calculated by various methods: ——, expression (2); ○○○, $-\nu\,\partial u/\partial r|_{r=R}$; · · · · ·, $\overline{u'v'}$ at $y/R = 0.1$; —●—, laminar theory or quasi-steady turbulence correlation.

Two checks can be applied to these measurements: (i) Throughout the cycle, the value of u_*^2 should agree with the quantity $-\nu\,\partial\bar{u}/\partial r|_{r=R}$. This quantity can readily be calculated from the LDA measurements of velocity and is also shown in figure 7. (ii) As will be discussed in more detail in §3.2.5, for the turbulent portion of the cycle, a constant stress layer exists near the wall ($y/R \ll 1$). In the outer portion of this region (i.e. for $y^+ = yu_*/\nu \gg 1$) the contribution of the viscous stresses to the overall local stress is small and the relation $\overline{u'v'}/u_*^2 \approx 1$ holds. The Reynolds stress for $y/R = 0.1$ ($y^+ \approx 35-70$) is also plotted in figure 7, and is seen to be in close agreement with u_*^2 in the turbulent portion of the cycle.

Also shown in figure 7, are two calculated curves of τ_w/ρ. The curves shown during the acceleration phase represent τ_w/ρ according to the solution of Uchida (1956) for laminar oscillatory flow in a pipe. For the deceleration phase, the displayed curves represent τ_w/ρ calculated from the Blasius correlation

$$\frac{\tau_w}{\rho} = 0.033\,25 u_{av}^2(\omega t)\left(\frac{\nu}{R u_{av}(\omega t)}\right)^{-0.25}$$

which applies to steady turbulent flows in smooth pipes. As can be see in figure 7, This correlation agrees surprisingly well with the measurements of τ_w/ρ, indicating that at least for flows in the range of parameters of this study ($u_*/\omega R \sim 1$) quasi-steady correlations can be used to predict the wall-friction velocities during the turbulent portion of the cycle.

3.2.3. *Logarithmic plots of ensemble-averaged velocity distributions*

Semi-logarithmic plots of ensemble-averaged velocity distributions, non-dimensionalized with respect to the corresponding wall-shear velocities, are displayed in figure 8 as a function of the wall coordinates $y^+ = yu_*/\nu$ for the case $Re^\delta = 1080$, $\Lambda = 10.6$. These plots indicate that the velocity profile during the deceleration phase of (*a*) Acceleration phase

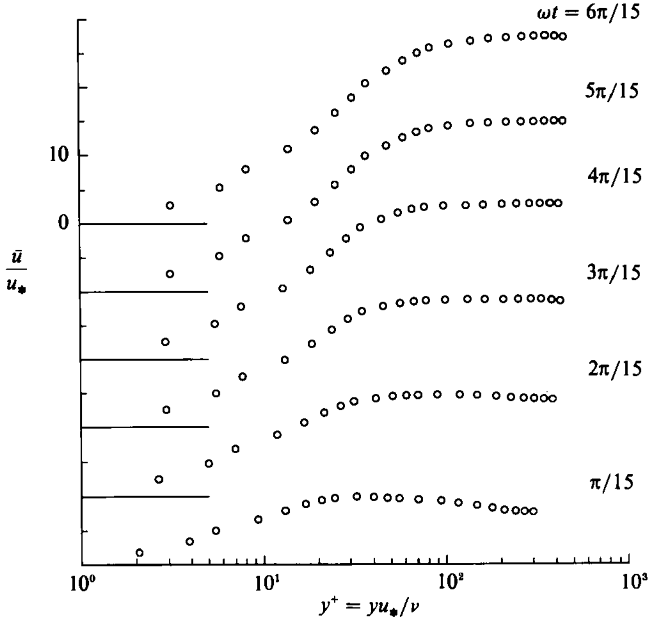

(*b*) Deceleration phase

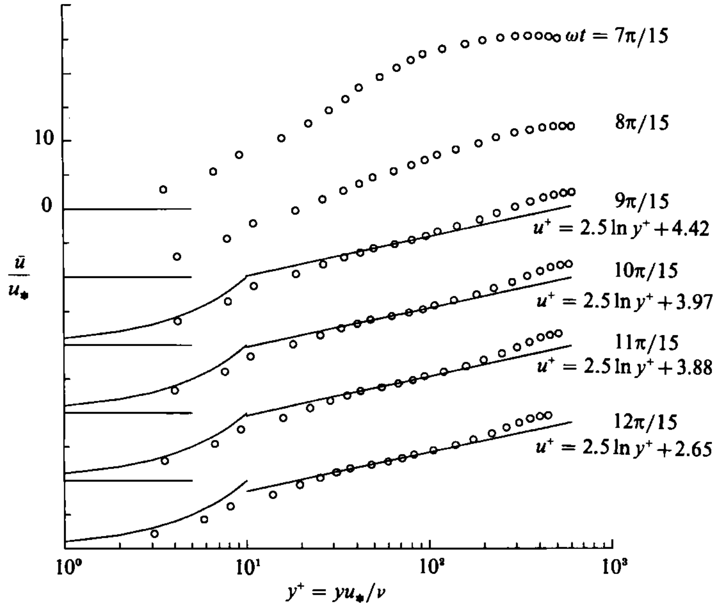

FIGURE 8(*a*, *b*). Semi-logarithmic plots of ensemble-averaged axial velocity in the turbulent flow regime. ($Re^\delta = 1080$, $\Lambda = 10.6$.)

the cycle is composed of a viscous sublayer, a logarithmic layer and an outer wake as for 'steady' turbulent wall-bounded flows. This behaviour is predicted by similarity arguments which show that the existence of a logarithmic layer is a dimensional necessity whenever at least two of the lengthscales R, u_*/ω and ν/u_* are widely separated, with the detailed structure of the flow being dependent upon the parameters $u_*/R\omega$ and $u_*^2/\omega\nu$.

To proceed with these similarity arguments, note that the dynamics of the flow at each phase during the turbulent portion of the cycle is governed by the parameters ρ, μ, R, ω and $u_*(\omega t)$. Three independent lengthscales can be formed from the indicated list of dimensional parameters; namely, a viscous lengthscale $\delta_\nu = \nu/u_*$, an unsteadiness lengthscale $\delta_t = u_*/\omega$ and a geometric lengthscale R. Dimensional analysis yields the following result for the ensemble-averaged velocity profiles $\bar{u}(y, \omega t)$ and moments of turbulent velocity fluctuations $\langle u'^k v'^l w'^m \rangle$:

$$\frac{\bar{u}}{u_*} = \Phi\left(\frac{yu_*}{\nu}, \frac{y\omega}{u_*}, \frac{y}{R}\right), \tag{3}$$

$$\frac{\langle u'^k v'^l w'^m \rangle}{u_*^{k+l+m}} = \phi_{klm}\left(\frac{yu_*}{\nu}, \frac{y\omega}{u_*}, \frac{y}{R}\right). \tag{4}$$

The relative magnitudes of the three lengthscales δ_ν, δ_t and R determines the structure of the flow. In what follows we assume that $Re_* = u_* R/\nu \gg 1$ so that $R \gg \delta_\nu$. Then, depending on the magnitude of δ_t, four different cases may be conceived.

Case I: $\delta_t \gg R \gg \delta_\nu \quad (u_*/\omega R \gg 1, Ru_*/\nu \gg 1)$

This case represents what might be called 'quasi-steady' turbulent behaviour. In this case, the influence of the lengthscale δ_t (representing effects of flow oscillation) is negligible for y in the range $0 < y < R$; i.e. throughout the cross-section of the pipe. The structure of the flow at each phase is determined by the two scales R and δ_ν, similar to 'steady' turbulent wall flows.

The detailed structure of the flow can be determined by the usual classical arguments, which utilize the fact that in the vicinity of the wall ($y \ll R$) the influence of the lengthscale R should also be negligible, so that

$$\frac{\bar{u}}{u_*} = \Phi_1\left(\frac{yu_*}{\nu}\right) = \Phi_1(y^+), \quad \frac{y}{u_*}\frac{\partial \bar{u}}{\partial y} = y^+ \frac{\partial \Phi_1}{\partial y^+}, \tag{5}$$

$$\frac{\langle u'^k v'^l w'^m \rangle}{u_*^{k+l+m}} = \phi_{klm}^{(1)}\left(\frac{yu_*}{\nu}\right). \tag{6}$$

Since $\nu \, \partial \bar{u}/\partial y|_{y=0} = u_*^2$, it is clear that to leading order $\Phi(y^+) \approx y^+$ for $y^+ \ll 1$.

In contrast, away from the wall ($y \gg \delta_\nu$), the fluid motion should be independent of the lengthscale δ_ν and

$$\frac{\bar{u} - \bar{u}_0}{u_*} = \Phi_2\left(\frac{y}{R}\right) = \Phi_2(Y), \quad \frac{y}{u_*}\frac{\partial \bar{u}}{\partial y} = Y\frac{\partial \Phi_2}{\partial Y}, \tag{7}$$

$$\frac{\langle u'^k v'^l w'^m \rangle}{u_*^{k+l+m}} = \phi_{klm}^{(2)}(y/R), \tag{8}$$

where $\bar{u}_0(wt)$ is the ensemble-averaged centreline velocity.

In the overlap region $\delta_\nu \ll y \ll R$, both sets of equations (5), (6) and (7), (8) should be simultaneously valid. It follows that, in this region,

$$y^+ \frac{\partial \Phi_1}{\partial y^+} = Y \frac{\partial \Phi_2}{\partial Y} = \text{const.} = A,$$

$$\phi^{(1)}_{klm}(y^+) = \phi^{(2)}_{klm}(Y) = \text{const.} = a_{klm},$$

leading (i) to a region of constant stress, and (ii) to a logarithmic form for both functions $\Phi_1(y^+)$ and $\Phi_2(Y)$ in the overlap region:

$$\frac{\bar{u}}{u_*} = A \ln\left(\frac{yu_*}{\nu}\right) + B, \tag{9}$$

$$\frac{\bar{u}-\bar{u}_0}{u_*} = A \ln\left(\frac{y}{R}\right) + B_1. \tag{10}$$

Thus in the regime for which $u_*/R\omega \gg 1$ and $u_* R/\nu \gg 1$ the universal log law applies and the flow behaves in a quasi-steady manner.

Case II: $\delta_t \sim R \gg \delta_\nu \quad (u_*/\omega R \sim 1, Ru_*/\nu \gg 1)$

Since δ_t is of the same order of magnitude as R, neither could affect the flow in the vicinity of the wall ($y \ll R$) and the usual law of the wall represented by (5), (6) is valid in this region. However, away from the wall ($y \gg \delta_\nu$) the fluid motion is influenced by both scales R and δ_t,

$$\frac{\bar{u}-\bar{u}_0}{u_*} = \Phi_2\left(\frac{y\omega}{u_*}, \frac{y}{R}\right) = \Phi_2(y_t, Y), \tag{11}$$

from which

$$\frac{y}{u_*}\frac{\partial \bar{u}}{\partial y} = y_t \frac{\partial \Phi_2}{\partial y_t} + Y \frac{\partial \Phi_2}{\partial Y},$$

and

$$\frac{\langle u'^k v'^l w'^m \rangle}{u_*^{k+l+m}} = \phi^{(2)}_{klm}\left(\frac{y\omega}{u_*}, \frac{y}{R}\right). \tag{12}$$

In the overlap region $\delta_\nu \ll y \ll R$, both sets of equations (5), (6) and (11), (12) should be valid and

$$y^+ \frac{\partial \Phi_1}{\partial y^+} = y_t \frac{\partial \Phi_2}{\partial y_t} + Y \frac{\partial \Phi_2}{\partial Y} = \text{const.} = A,$$

$$\phi^{(1)}_{klm}(y^+) = \phi^{(2)}_{klm}(y_t, Y) = \text{const.} = a_{klm}.$$

This leads to the modified logarithmic law

$$\frac{\bar{u}}{u_*} = A \ln\left(\frac{yu_*}{\nu}\right) + B', \tag{13}$$

$$\frac{\bar{u}-\bar{u}_0}{u_*} = A \ln\left(\frac{y}{R}\right) + B_2\left(\frac{u_*}{R\omega}\right), \tag{14}$$

where the coefficient B_2 (and hence B') now depends on the parameter $u_*/R\omega$. Since u_* is a function of ωt, the velocity profiles in this regime obey a logarithmic law with the same slope as the universal low law but with an intercept that varies with ωt. The experimental data reported in figure 8(*b*) belong to this regime. For the flow shown in figure 8(*b*), the value of $u_*/R\omega$ during the deceleration phase ranged from 2.8 at

$\omega t = \frac{1}{2}\pi$ to 1.0 at $\omega t = 14\pi/15$, with Ru_*/ν varying between 630 and 240 for the same period. Accordingly, during this period, the experimental velocity profiles can be described by $\bar{u}/u_* = y^+$ for $y^+ < 10$ and by $\bar{u}/u_* = A \ln y^+ + B(\omega t)$ for $30 < y^+ < 200$. The slope A in the semi-logarithmic distribution of velocity has a value of 2.5 which corresponds to a von Kármán constant of $\kappa = 0.4$. The value of B, however, is a function of the phase in the cycle and varies between 2.5 and 4.5 (compared to $B = 5.5$ for steady pipe flows).

Case III: $R \gg \delta_t \gg \delta_\nu \quad (u_*/\omega R \ll 1,\ u_*^2/\omega\nu \gg 1)$

Once again, near the wall ($y \ll \delta_t$) the only scale affecting the flow is δ_ν and the usual law of the wall (5), (6), is valid in this region. Moreover, the scales δ_ν and R are unimportant for $\delta_\nu \ll y \ll R$,

$$\frac{\bar{u}}{u_*} = \Phi_2\left(\frac{y\omega}{u_*}\right) = \Phi_2(y_t), \quad \frac{y}{u_*}\frac{\partial \bar{u}}{\partial y} = y_t \frac{\partial \Phi_2}{\partial y_t}, \tag{15}$$

$$\frac{\langle u'^k v'^l w'^m \rangle}{u_*^{k+l+m}} = \phi_{klm}^{(2)}\left(\frac{y\omega}{u_*}\right). \tag{16}$$

In the overlap region $\delta_\nu \ll y \ll \delta_t$ both sets of equations (5), (6) and (15), (16) should be simultaneously valid. Therefore, in this region,

$$y^+ \frac{\partial \Phi_1}{\partial y^+} = y_t \frac{\partial \Phi_2}{\partial y_t} = \text{const.} = A, \quad \phi_{klm}^{(1)}(y^+) = \phi_{klm}^{(2)}(y_t) = \text{const.} = a_{klm},$$

leading to the usual region of constant moments and logarithmic velocity profiles within this layer.

In the outer region ($y \gg \delta_t$) neither of the scales δ_ν or δ_t can affect the flow. However, the usual velocity defect law (7) is not valid in this region. This is because passage to the limit $y/\delta_t \rightarrow \infty$ (i.e. $\delta_t = u_*/\omega \rightarrow 0$) is equivalent to flow conditions where $u_* \rightarrow 0$ but where ω remains finite. Therefore, in the region $y \gg \delta_t$ the parameters R and ω (but not ν or u_*) should be relevant. This leads to

$$\frac{\bar{u} - \bar{u}_0}{R\omega} = \Phi_3\left(\frac{y}{R}\right), \tag{17}$$

$$\langle u'^k v'^l w'^m \rangle = (R\omega)^{k+l+m}\, \phi_{klm}^{(3)}\left(\frac{y}{R}\right), \tag{18}$$

indicating that in oscillatory flows where $u_*/R\omega \ll 1$ and $u_*^2/\omega\nu \gg 1$, the fluid behaves in an inviscid manner in the outer region and turbulent moments remain frozen during the cycle in this outer region.

Our experiments did not extend to such high frequencies that the conditions $u_*/R\omega \ll 1$, $u_*^2/\omega\nu \gg 1$ could be satisfied for a significant portion of the deceleration phase in any of our runs. However, Mizushima *et al.* (1975) and Ramaprian & Tu (1983) have both reported measurements for turbulent oscillatory flow about a non-zero flow with $u_*/R\omega \approx 0.1$, $u_*^2/\omega\nu \approx 100$ and the features reported by them are consistent with the predictions of the similarity analysis described above.

Case IV: $R \gg \delta_t \sim \delta_\nu \quad (u_*/\omega R \ll 1,\ u_*^2/\omega\nu \sim 1)$

Here the effect of oscillation is confined to the near-wall region ($y \ll R$), as evidenced by the fact that δ_t cannot affect the flow away from the wall. In the near-wall region

$$\frac{\bar{u}}{u_*} = \Phi_1\left(\frac{yu_*}{\nu}, \frac{y\omega}{u_*}\right) = \Phi_1(y^+, y_t), \quad \frac{y}{u_*}\frac{\partial \bar{u}}{\partial y} = y^+\frac{\partial \Phi_1}{\partial y^+} + y_t\frac{\partial \Phi_1}{\partial y_t}, \tag{19}$$

$$\frac{\langle u'^k v'^l w'^m \rangle}{u_*^{k+l+m}} = \phi^{(1)}_{klm}\left(\frac{yu_*}{\nu}, \frac{y\omega}{v_*}\right). \tag{20}$$

Whereas in the core ($y \gg \delta_\nu$), the usual velocity defect law (7), (8) holds. The overlap region between (7), (8) and (19), (20) leads to the modified logarithmic law

$$\frac{\bar{u}}{u_*} = A \ln\left(\frac{yu_*}{\nu}\right) + B_3\left(\frac{u_*^2}{\omega\nu}\right), \tag{21}$$

$$\frac{\bar{u}-\bar{u}_0}{u_*} = A \ln\left(\frac{y}{R}\right) + B_4, \tag{22}$$

with the same slope as the universal log law, but with an intercept that may vary with ωt. No experimental data are presently available for flow in this regime.

In connection with the four flow regimes described above, we should also mention a similar classification of turbulent oscillatory flows (in terms of the parameter $u_*/R\omega$) that has been suggested by Ramaprian & Tu (1983). The similarity arguments outlined above, in general, predict many of the features that were described by Ramaprian & Tu (1983) for flow in each regime, and furthermore demonstrate the significance of the additional parameter $u_*^2/\omega\nu$ in determining the structure of the flow.

3.2.4. *Turbulence intensities*

The turbulence intensities ($(\overline{u'^2})^{\frac{1}{2}}$ and $(\overline{v'^2})^{\frac{1}{2}}$) and the turbulent shear stress ($\overline{u'v'}$) are defined as

$$(\overline{u'^2})^{\frac{1}{2}} = \left\{\frac{1}{N}\sum_{j=1}^{N} u_j'^2(r, \omega t + 2\pi(j-1))\right\}^{\frac{1}{2}}, \tag{23}$$

$$(\overline{v'^2})^{\frac{1}{2}} = \left\{\frac{1}{N}\sum_{j=1}^{N} v_j'^2(r, \omega t + 2\pi(j-1))\right\}^{\frac{1}{2}}, \tag{24}$$

$$\overline{u'v'} = \frac{1}{N}\sum_{j=1}^{N} u_j'(r, \omega t + 2\pi(j-1))\, v_j'(r, \omega t + 2\pi(j-1)), \tag{25}$$

where u' and v' are the differences between the instantaneous and the ensemble-averaged velocities,

$$u'(r, \omega t) = u(r, \omega t) - \bar{u}(r, \omega t), \tag{26}$$

$$v'(r, \omega t) = v(r, \omega t) - \bar{v}(r, \omega t). \tag{27}$$

The phase variation of axial and radial turbulence intensities ($(\overline{u'^2})^{\frac{1}{2}}$, $(\overline{v'^2})^{\frac{1}{2}}$) at various radial positions across the pipe are shown in figure 9. During the early part of the acceleration phase, turbulence intensities remain at a low level in both the radial and axial directions. During this period, both quantities have a fairly uniform distribution across the pipe cross-section and no significant variation in the level of disturbances can be detected as a function of the phase in the cycle. In absolute magnitude, however, axial turbulence intensities are always roughly twice as large as radial intensities (see also figure 11).

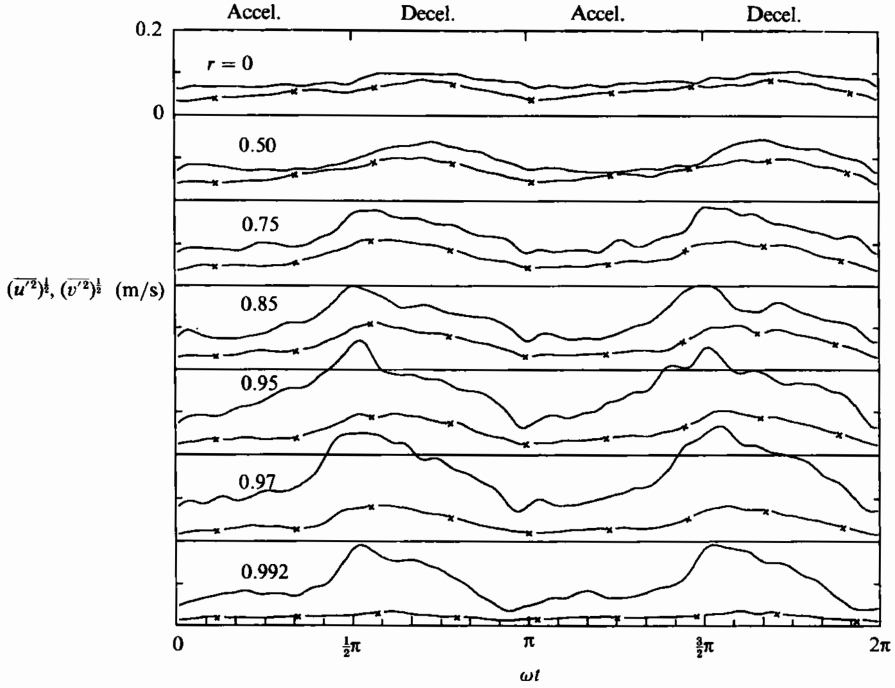

FIGURE 9. Phase variation of axial (——) and radial (—×—) turbulence intensities at various radial locations. ($Re^\delta = 1080$, $\Lambda = 10.6$.)

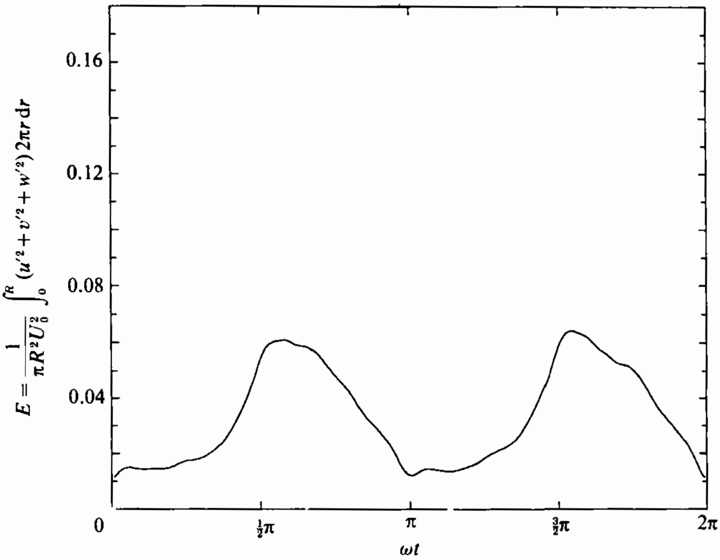

FIGURE 10. Phase variation of overall kinetic energy of disturbances, normalized to that of the mean flow. ($Re^\delta = 1080$, $\Lambda = 10.6$.)

Shortly before the start of the deceleration phase, at a time $\omega t \sim 5\pi/12$, turbulence intensities in both the radial and axial directions rapidly increase over a very short (convective) timescale. For the axial component, the increase occurs most prominently in the near-wall region; whereas for the radial component, the increase

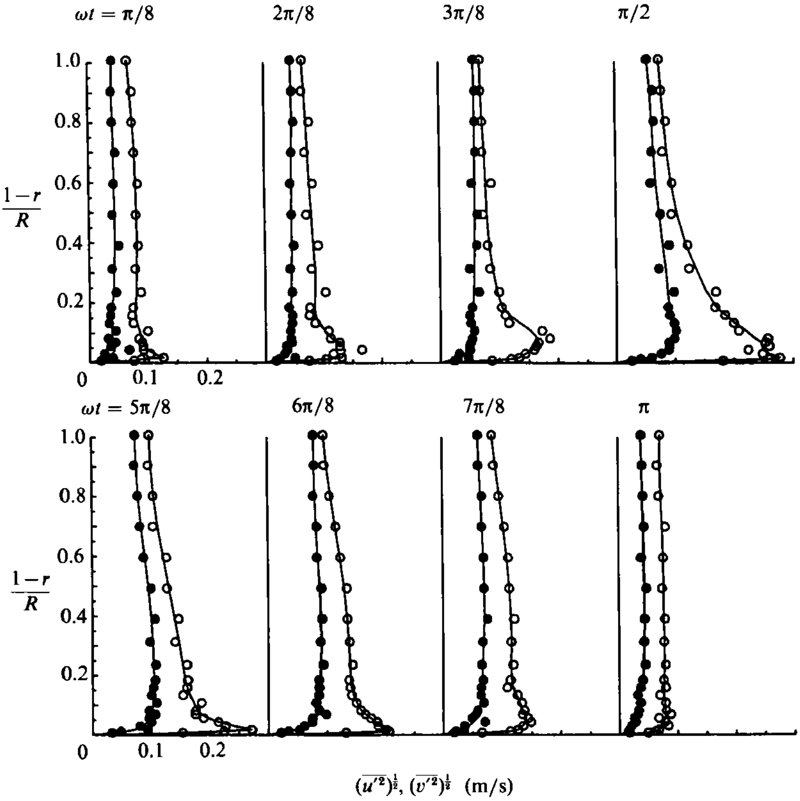

FIGURE 11. Distributions of axial (—o—) and radial (—●—) turbulence intensities across the pipe cross-section. ($Re^{\delta} = 1080$, $\Lambda = 10.6$.)

is more uniform throughout the cross-section of the pipe. The comparison between the timescale of appearance of turbulence and the timescale of variation of the flow is best seen in figure 10, where the overall kinetic energy of the fluctuations integrated over the cross-section of the pipe (and normalized to that of the mean flow) is plotted as a function of the phase in the cycle. The short (explosive) timescale for the appearance of turbulence towards the end of the acceleration phase indicates that turbulence is generated by a snap-through transition mechanism. From figure 10 it can also be seen that during the early part of the acceleration phase the disturbances retain a finite energy, even though production of turbulence has dropped to very low levels (figure 18). These features are in agreement with the flow visualization studies of Hayashi & Ohashi (1981), where it was observed that with the start of the acceleration phase a large-scale structure of eddies would form which was convected by the mean flow with little distortion.

The distributions of axial and radial turbulence intensities $((\overline{u'^2})^{\frac{1}{2}}, (\overline{v'^2})^{\frac{1}{2}})$, as well as the ratio of the turbulence intensities to the ensemble-averaged centreline velocity $((\overline{u'^2})^{\frac{1}{2}}/\bar{u}_0, (\overline{v'^2})^{\frac{1}{2}}/\bar{u}_0)$, are plotted in figures 11 and 12 for various phases during the cycle. Comparison with earlier measurements of these quantities in steady pipe flows (Laufer 1954) shows that the structure and distribution of turbulence intensities for the present case is essentially identical to that for steady wall-bounded flows. Turbulence is nearly isotropic near the centre of the pipe, while in the wall region axial turbulence intensities are 2.5 to 3 times the radial intensities, similar to steady

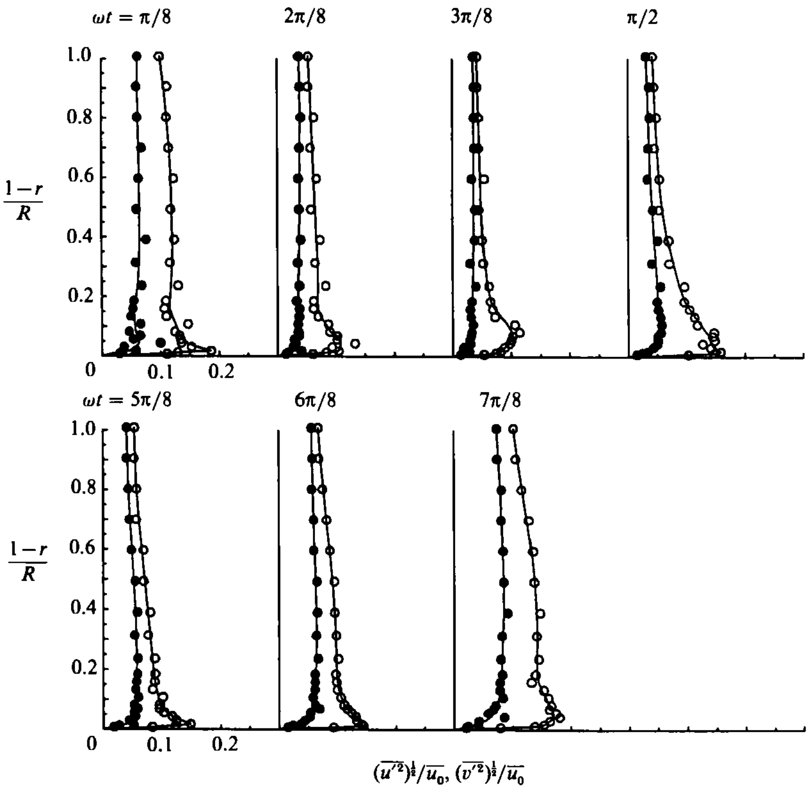

FIGURE 12. Distributions of axial (—○—) and radial (—●—) turbulence intensities normalized to ensemble-averaged centreline velocities, across the pipe cross-section. ($Re^\delta = 1080$, $\Lambda = 10.6$.)

turbulent pipe flows. The major difference from steady flow results is in the ratio of turbulence intensities to the ensemble-averaged centreline velocity (figure 12). In the present experiments, this ratio for both axial and radial turbulence intensities was twice as large as that reported for steady pipe flows (Laufer 1954). This indicates that, for oscillating flows, turbulence is generated more vigorously than for steady flows with zero pressure gradient.

Figures 11 and 12 do not provide a detailed description of the distribution of turbulence intensities in the near-wall region. To see these regions in more detail, the ratios $(\overline{u'^2})^{\frac{1}{2}}/u_*$ and $(\overline{v'^2})^{\frac{1}{2}}/u_*$ are plotted *vs.* the wall coordinate y^+, for $y^+ \leqslant 200$ in figure 13. As seen in this figure, $(\overline{u'^2})^{\frac{1}{2}}$ reaches a peak value of $\approx 4u_*$ near $y^+ \approx 10$. This should be compared to the peak ratio $(\overline{u'^2})^{\frac{1}{2}}/u_* \approx 2.5$ at $y^+ \approx 15$ for steady wall-bounded flows.

3.2.5. *Turbulent shear stresses*

The phase variation of the turbulence shear stress $\overline{u'v'}$ for various radial locations is shown in figure 14. During the early part of the acceleration phase of the cycle, turbulent shear stresses (and hence the rates of turbulence energy production, $\overline{u'v'}\,\partial\tilde{u}/\partial r$) are negligibly small throughout the pipe. However, towards the end of the acceleration phase there is a rapid buildup of turbulent shear stresses in the near-wall region of the pipe.

Distributions of absolute and normalized turbulent shear stresses ($\overline{u'v'}$ and

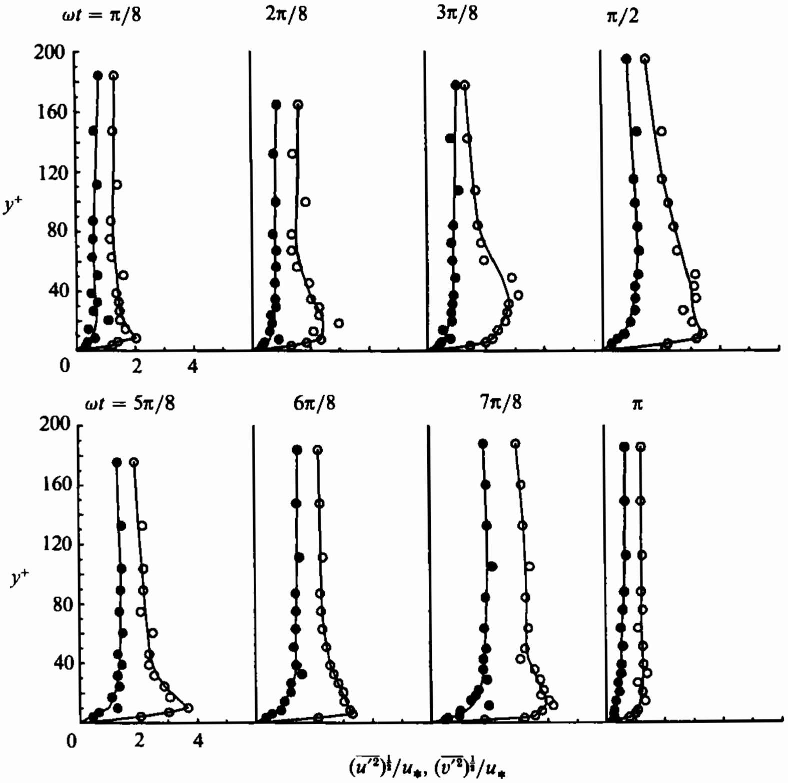

FIGURE 13. Distributions of axial (—○—) and radial (—●—) turbulence intensities normalized to ensemble-averaged wall-friction velocities, in the near-wall region. ($Re^\delta = 1080$, $\Lambda = 10.6$.)

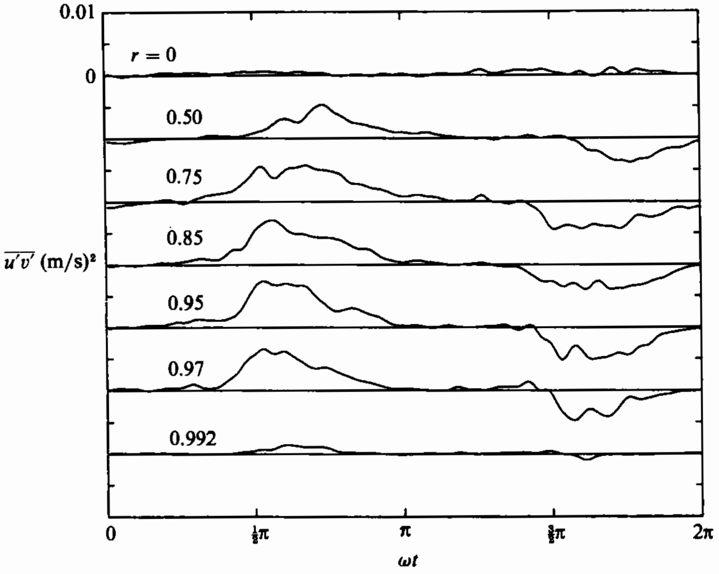

FIGURE 14. Phase variation of turbulent shear stresses at various radial locations. ($Re^\delta = 1080$, $\Lambda = 10.6$.)

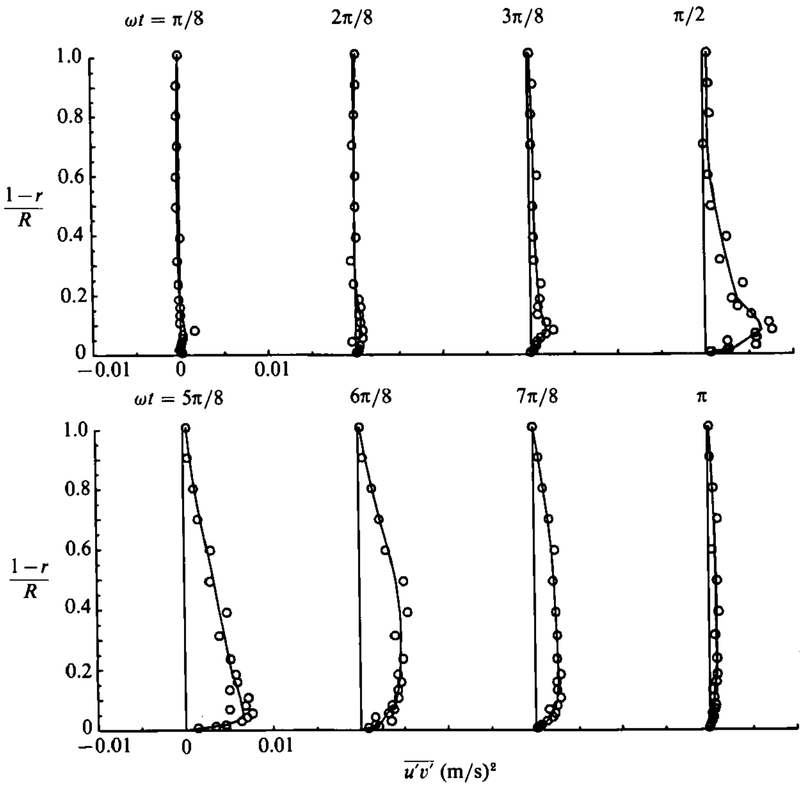

FIGURE 15. Distribution of turbulent shear stress across the pipe cross-section for various phases. ($Re^{\delta} = 1080$, $\Lambda = 10.6$.)

$\overline{u'v'}/u_*^2$) across the pipe cross-section are shown in figures 15 and 16 for selected phases during the cycle. The turbulent shear stress at a location r is given by

$$\overline{u'v'} - \nu\frac{\partial \bar{u}}{\partial r} = \frac{r}{2}\left(-\frac{1}{\rho}\frac{\partial \bar{p}}{\partial x}\right) - \frac{1}{r}\int_0^r \frac{\partial \bar{u}}{\partial t} r\,\mathrm{d}r.$$

Substituting for $-1/\rho(\partial\bar{p}/\partial x)$ from (2), results in

$$\overline{u'v'} - \nu\frac{\partial \bar{u}}{\partial r} = \frac{r}{R}(u_*^2) + \left(\frac{r}{R}\right)\frac{1}{R}\int_0^R \frac{\partial \bar{u}}{\partial t} r\,\mathrm{d}r - \frac{1}{r}\int_0^r \frac{\partial \bar{u}}{\partial t}\bar{u}r\,\mathrm{d}r.$$

Away from the wall $\nu\,\partial\bar{u}/\partial r$ is negligible and the above equation reduces to

$$\frac{\overline{u'v'}}{u_*^2} \approx \frac{r}{R} + \left(\frac{r}{R}\right)\frac{1}{Ru_*^2}\frac{\partial}{\partial t}\int_0^R \bar{u}r\,\mathrm{d}r - \frac{1}{ru_*^2}\int_0^r \bar{u}r\,\mathrm{d}r. \tag{28}$$

In the core, where $\bar{u}$ is nearly uniform, this reduces to

$$\frac{\overline{u'v'}}{u_*^2} \approx \frac{r}{R}.$$

In contrast, for the region near the wall such that $y/R \ll 1$, but still outside of the

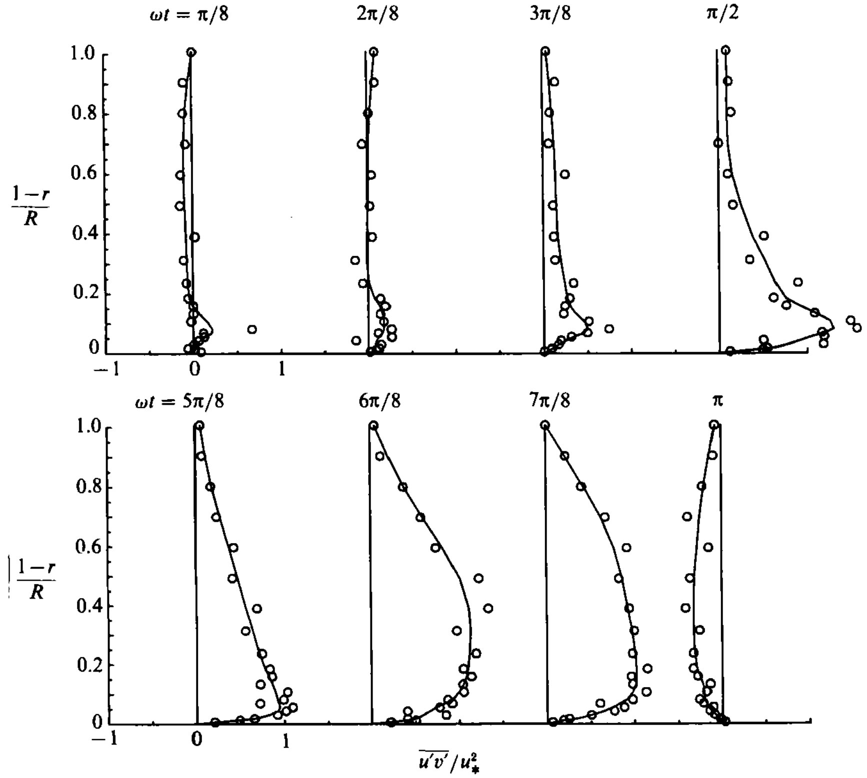

FIGURE 16. Distribution of turbulent shear stress, normalized to wall-friction velocity, across the pipe cross-section for various phases. ($Re^\delta = 1080$, $A = 10.6$.)

viscous sublayer so that the viscous stresses are still negligible (i.e. for $\delta_\nu \ll y/R \ll 1$), (28) reduces to

$$\frac{\overline{u'v'}}{u_*^2} \approx 1,$$

indicating that a layer of constant Reynolds stress exists near the wall.

The two layers ($\overline{u'v'}/u_*^2 \approx r/R$ in the core, and $\overline{u'v'}/u_*^2 \approx 1$ near the wall) can be distinctly seen in the plots of figure 16 for most of the deceleration phase of the cycle.

In figure 16, $\overline{u'v'}/u_*^2$ becomes negative for $\omega t = \pi$. This simply is a reflection of the reversal of flow in the near-wall region at this phase (in our notation, $\tau_w/\rho = u_*^2$ takes on negative values for $\pi \leqslant \omega t < 2\pi$). It does not imply production of negative stresses (see figure 15).

3.2.6. *Turbulence energy production*

Profiles of the rates of turbulence energy production, $-\rho\overline{u'v'}\,\partial\bar{u}/\partial y$, are displayed in figure 17 for a turbulent flow at $Re^\delta = 1080$, $A = 10.6$. Production of turbulence is most significant during the late stages of the acceleration phase and early stages of the deceleration phase and has its peak value at $y^+ \approx 10$, similar to steady wall-bounded turbulent flows (Laufer 1954).

The overall rate of turbulence energy production, integrated over the pipe cross-section, is shown in figure 18. Significant production of turbulence occurs only during

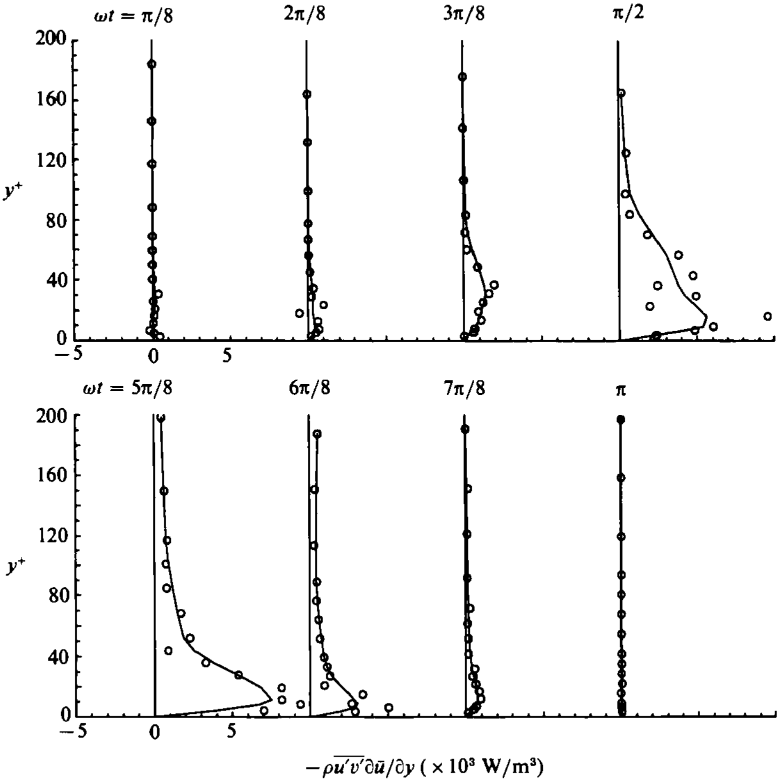

FIGURE 17. Profiles of the rates of turbulence energy production near the wall for various phases during the cycle. ($Re^{\delta} = 1080$, $A = 10.6$.)

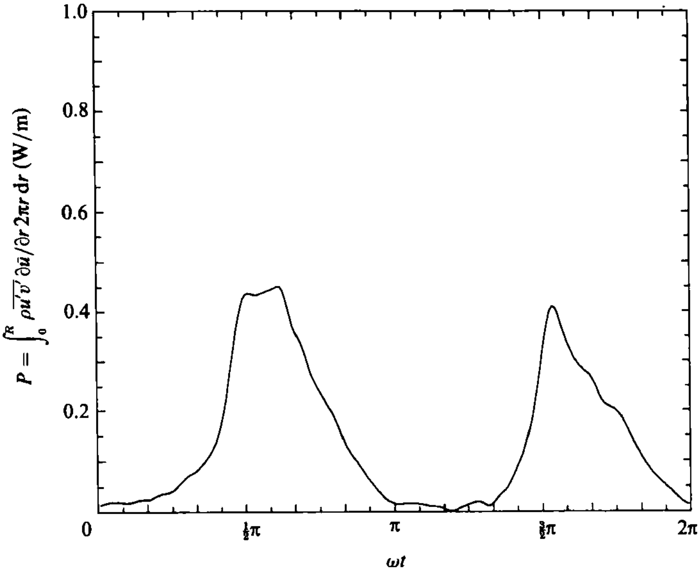

FIGURE 18. Phase variation of the overall rate of turbulence energy production across the pipe cross-section. ($Re^{\delta} = 1080$, $A = 10.6$.)

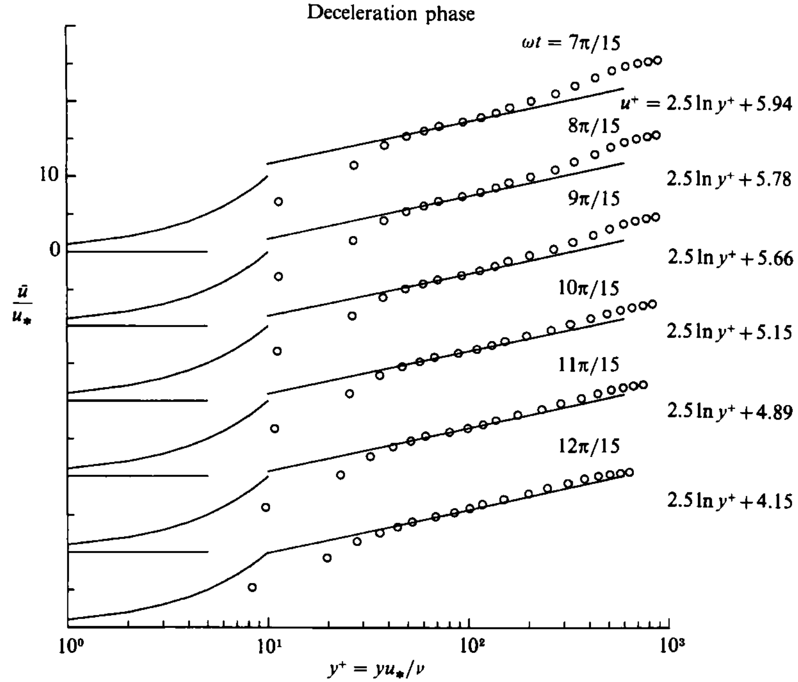

FIGURE 19. Semi-logarithmic plots of ensemble-averaged axial velocity in the turbulent flow regime. ($Re^\delta = 1720$, $\Lambda = 10.6$.)

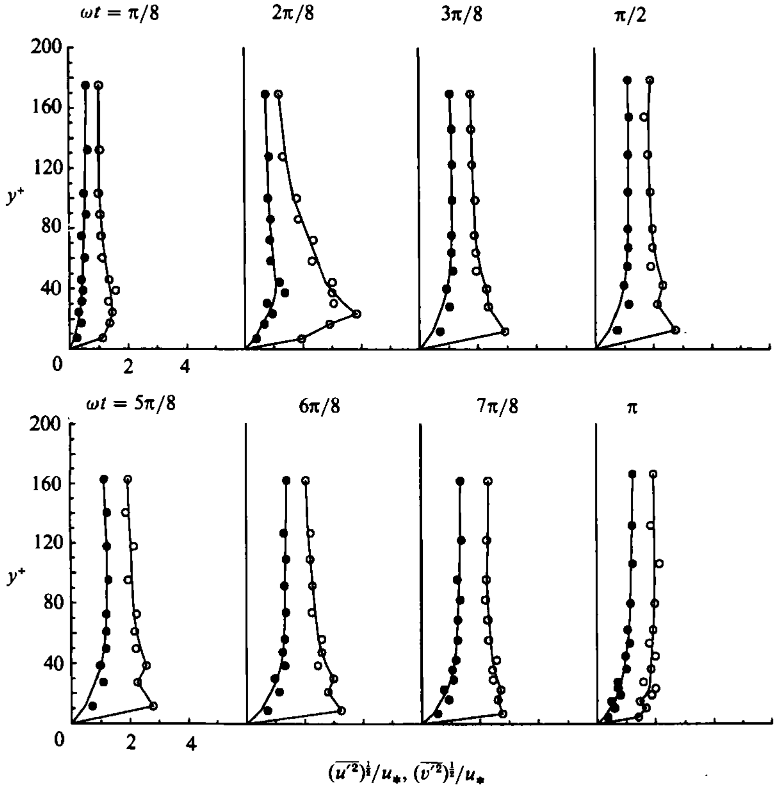

FIGURE 20. Distributions of axial (—o—) and radial (—●—) turbulence intensities, normalized to instantaneous wall-friction velocities, in the near-wall region. ($Re^\delta = 1720$, $\Lambda = 10.6$.)

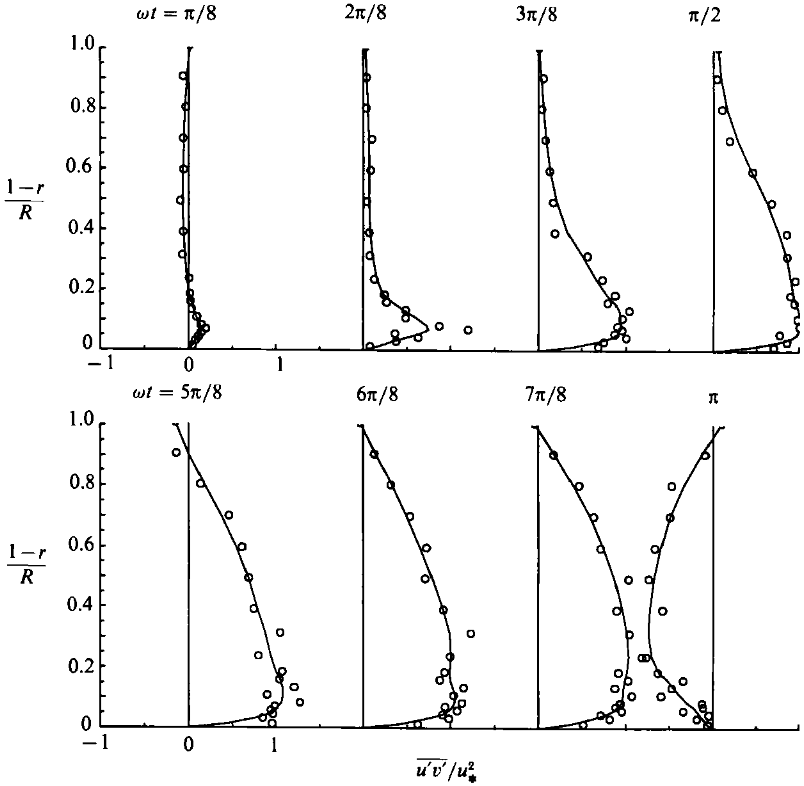

FIGURE 21. Distribution of turbulent shear stress, normalized to wall-friction velocity, across the pipe cross-section for various phases. ($Re^\delta = 1720$, $A = 10.6$.)

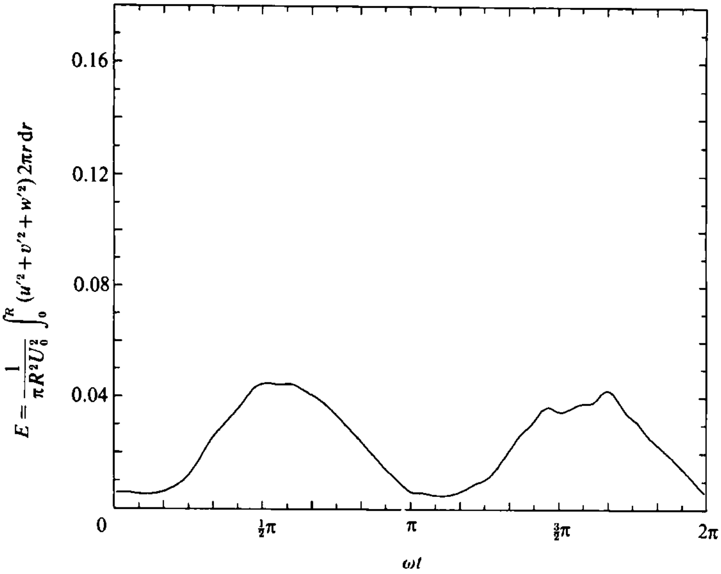

FIGURE 22. Phase variation of overall kinetic energy of disturbances, normalized to that of the mean flow. ($Re^\delta = 1720$, $A = 10.6$.)

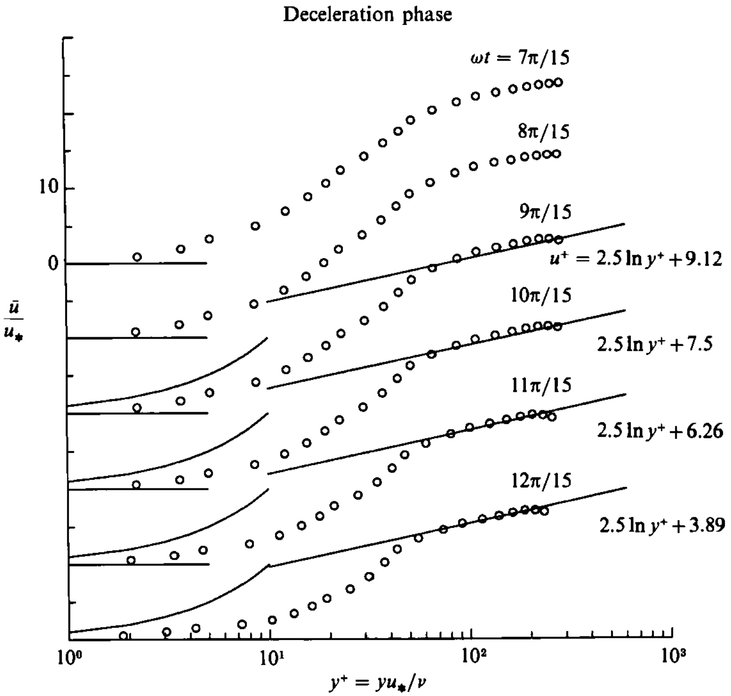
Deceleration phase

FIGURE 23. Semi-logarithmic plots of ensemble-averaged axial velocity in the turbulent flow regime. ($Re^\delta = 957$, $\Lambda = 5.7$.)

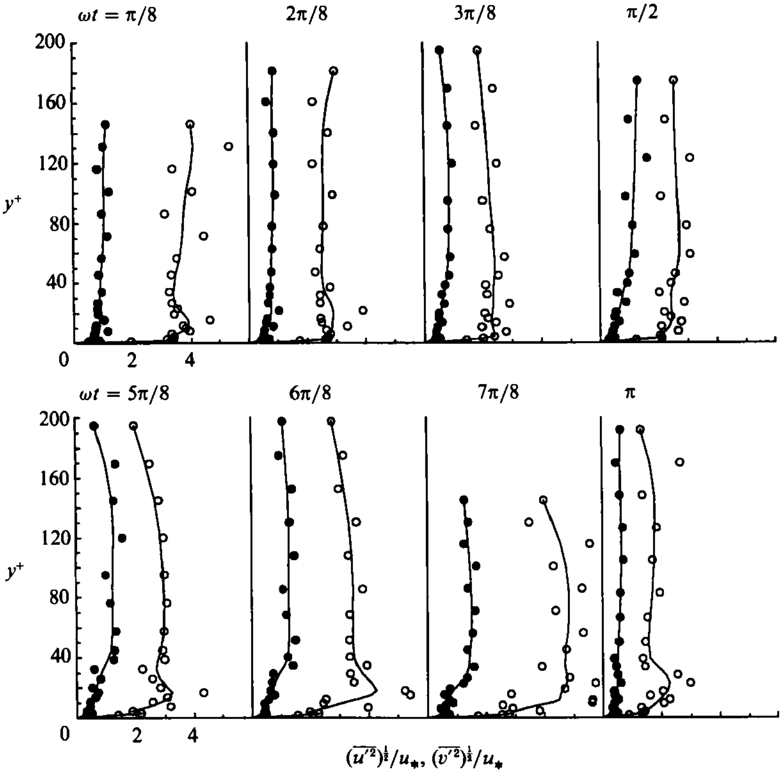

FIGURE 24. Distributions of axial (—o—) and radial (—●—) turbulence intensities, normalized to instantaneous wall-friction velocities, in the near-wall region. ($Re^\delta = 957$, $\Lambda = 5.7$.)

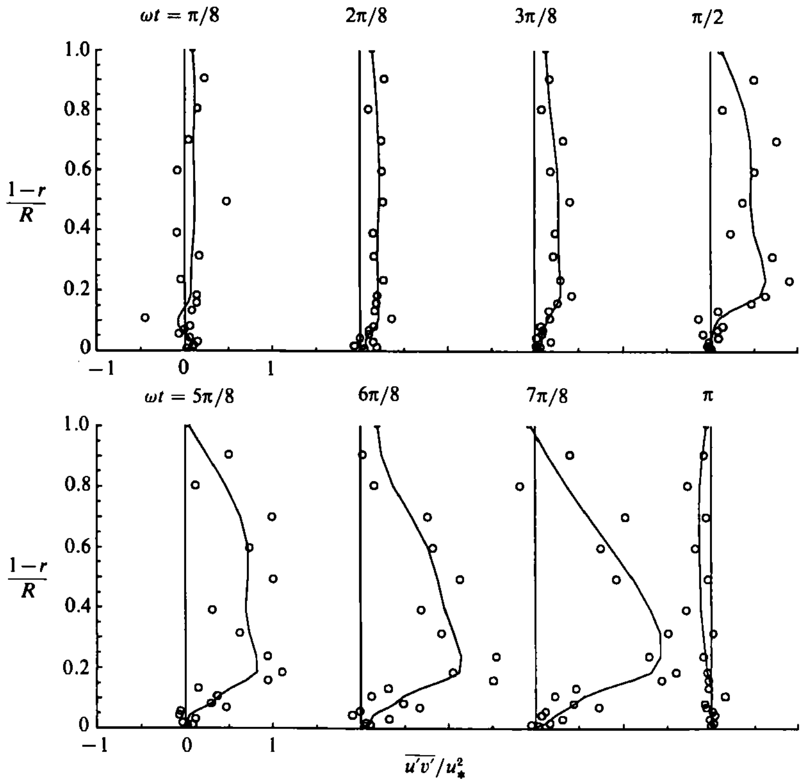

FIGURE 25. Distribution of turbulent shear stress normalized to wall-friction velocity, across the pipe cross-section for various phases. ($Re^\delta = 957$, $\Lambda = 5.7$.)

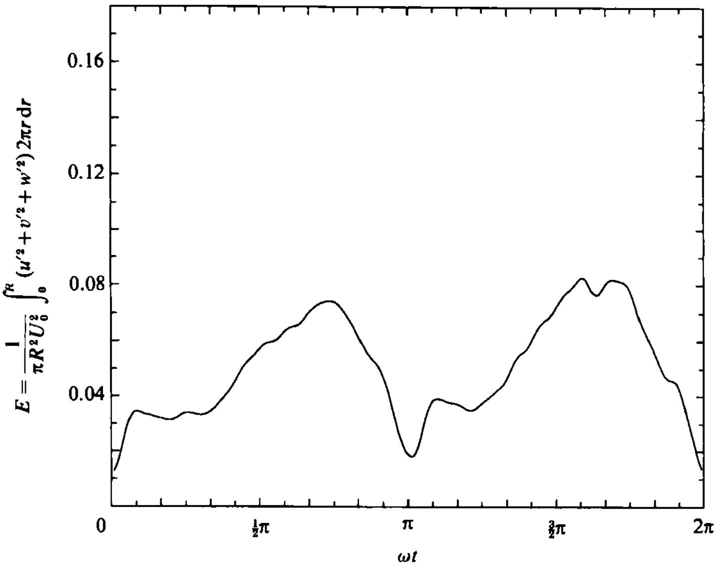

FIGURE 26. Phase variation of overall kinetic energy of disturbances, normalized with that of the mean flow. ($Re^\delta = 957$, $\Lambda = 5.7$.)

the late stages of the acceleration phase and the early stages of the deceleration phase of the cycle. During the early stages of the acceleration phase, production of turbulence essentially stops.

3.3. *Effect of Re^{δ} and Λ*

The features described in the previous sections were common to all the cases studied, which were all such that $u_*/R\omega \sim 1$ and $Ru_*/\nu \gg 1$ during the turbulent portion of the cycle; hence the description provided under case II applied to all flows. Representative plots of profiles of axial velocities, turbulence intensities, turbulent Reynolds stresses and overall kinetic energy of disturbances are shown in figures 19–22 for a flow at $Re^{\delta} = 1720$, $\Lambda = 10.6$. The major difference between this flow and the case $Re^{\delta} = 1080$, $\Lambda = 10.6$ discussed earlier, is that for flow at this higher Reynolds number turbulence sets in at an earlier stage during the cycle. The flow is turbulent for $\frac{1}{3}\pi < \omega t < \pi$ and for $\frac{4}{3}\pi < \omega t < 2\pi$, corresponding to the latter half of the acceleration phase and all of the deceleration phase (figure 22). During the turbulent portion of the cycle, the velocity profiles could be described by $u^+ = y^+$ for $y^+ < 10$ and $u^+ = A \ln y^+ + B(\omega t)$ for $30 < y^+ < 200$, with $A = 2.5$ and B varying between 5.94 and 4.15 (figure 19). As before, during the early part of the acceleration phase, production of turbulence stops and the flow reverts to laminar. For the turbulent portion of the cycle, production of turbulence is most significant around $y^+ \approx 10$ similar to the case discussed before and to steady wall-bounded turbulent flows. The overall kinetic energy of disturbances, integrated over the cross-section of the pipe and normalized with respect to that of the mean flow, is plotted in figure 22. Comparison with figure 10 shows that the disturbances seem to saturate at a peak energy of roughly 4 to 6% of the kinetic energy of the mean flow.

Similar results were also obtained for a flow at $Re^{\delta} = 957$, $\Lambda = 5.7$. These results are shown in figures 23–26. Compared to the case $Re^{\delta} = 1080$, $\Lambda = 10.6$, absolute rates of production of turbulence were significantly lower in this case. This is due to the lower value of ω which results in less severe adverse pressure gradients during the deceleration phase of the cycle. As a result, absolute magnitudes of wall-shear velocities were lower, and the inner scales extended further into the cross-section of the pipe. Once appropriately non-dimensionalized, however, the results agreed with the two cases discussed earlier.

4. Conclusions

The structure of oscillatory turbulent flow in a pipe has been studied by laser-Doppler velocimetry. In all flows studied, turbulence appeared explosively towards the end of the acceleration phase of the cycle and was sustained throughout the deceleration phase. During the early part of the acceleration phase, production of turbulence decreased to very low levels and the profiles agreed with laminar theory. Nevertheless, during this period the disturbances retained a small but finite energy. During the turbulent portion of the cycle, production of turbulence was restricted to the wall region of the pipe and was the result of turbulent bursts. The statistics of the resulting turbulent flow showed a great deal of similarity to results for steady wall-bounded turbulent shear flows, provided quantities were non-dimensionalized with respect to the corresponding ensemble-averaged wall-friction velocities. The two non-dimensional groups $u_*/R\omega$ and $u_*^2/\omega\nu$ have been identified as critical parameters in determining the structure of the flow, and have been used to classify oscillatory turbulent flows. The major features observed in these experiments are used as a guideline in Part 2 of this paper (Akhavan *et al.* 1991) to identify the nature of the instability that is most likely to be responsible for transition in these class of flows.

This work was supported by NSF grant MEA-8313017.

REFERENCES

AKHAVAN, R., KAMM, R. D. & SHAPIRO, A. H. 1991 An investigation of transition to turbulence in bounded oscillatory Stokes flows. Part 2. Numerical simulation. *J. Fluid Mech.* **225**, 423–444.

COLLINS, J. I. 1963 Inception of turbulence at the bed under periodic gravity waves. *J. Geophys. Res.* **18**, 6007–6014.

COWLEY, S. J. 1987 High frequency Rayleigh instability of Stokes layers. In *Stability of Time Dependent and Spatially Varying Flows* (ed. D. L. Dwoyer & M. Y. Hussaini), pp, 261–275. Springer.

HALL, P. 1978 The linear stability of flat Stokes layers. *Proc. R. Soc. Lond.* A **359**, 151–166.

HAYASHI, T. & OHASHI, M. 1981 A dynamical and visual study of the oscillatory turbulent boundary layer. In *Turbulent Shear Flows 3*, pp. 18–33. Springer.

HINO, M., KASHIWAYANAGI, M., NAKAYAMA, A. & HARA, T. 1983 Experiments on the turbulence statistics and the structure of a reciprocating oscillatory flow. *J. Fluid Mech.* **131**, 363–400.

HINO, M., SAWAMOTO, M. & TAKASU, S. 1976 Experiments on transition to turbulence in an oscillating pipe flow. *J. Fluid Mech.* **75**, 193–207.

KERCZEK, C. VON & DAVIS, S. H. 1974 Linear stability theory of oscillatory Stokes layers. *J. Fluid Mech.* **62**, 753–773.

LAUFER, J. 1954 The structure of turbulence in fully developed pipe flow. *Natl Advisory Comm. Aeronaut. Tech. Rept.* 1174.

LI, H. 1954 Stability of oscillatory laminar flow along a wall. *Beach Erosion Board, US Army Corps Engrs Tech. Memo* 47.

MARCHAND, P. & MARMET, L. 1983 Binomial smoothing filter: a way to avoid some pitfalls of least-squares polynomial smoothing. *Rev. Sci. Instrum.* **54**, 1034.

MERKLI, P. & THOMANN, H. 1975 Transition to turbulence in oscillating pipe flow. *J. Fluid Mech.* **68**, 567–575.

MIZUSHINA, T., MARUYAMA, T. & HIRASAWA, H. 1975 Structure of the turbulence in pulsating pipe flow. *J. Chem. Engng Japan* **8**, 210–216.

MIZUSHINA, T., MARUYAMA, T. & SHIOZAKI, Y. 1973 Pulsating turbulent flow in a tube. *J. Chem. Engng Japan* **6**, 487–494.

MONKEWITZ, P. A. & BUNSTER, A. 1987 The stability of the Stokes layer: visual observations and some theoretical considerations. In *Stability of Time Dependent and Spatially Varying Flows* (ed. D. L. Dwoyer & M. Y. Hussain), pp. 244–260. Springer.

OBREMSKI, H. J. & MORKOVIN, M. V. 1969 Application of a quasi-steady stability model to a periodic boundary layer flow. *AIAA J.* **7**, 1298–1301.

OHMI, M., IGUCHI, M., KAKEHACHI, K. & MASUDA, T. 1982 Transition to turbulence and velocity distribution in an oscillating pipe flow. *Bull. JSME* **25**, 365–371.

RAMAPRIAN, B. R. & TU, S. W. 1983 Fully developed periodic turbulent pipe flow. Part 2. The detailed structure of the flow. *J. Fluid Mech.* **137**, 59–81.

SERGEEV, S. I. 1966 Fluid oscillations in pipes at moderate Reynolds numbers. *Fluid Dyn.* **1**, 121–122.

TARDU, S., BINDER, G. & BLACKWELDER, R. 1987 Response of turbulence to large amplitude oscillations in channel flow. In *Advances in Turbulence* (ed. G. Comte-Bellot & J. Mathieu), pp. 564–555. Springer.

TU, S. W. & RAMAPRIAN, B. R. 1983 Fully developed periodic turbulent pipe flow. Part 1. Main experimental results and comparison with predictions. *J. Fluid Mech.* **137**, 31–58.

UCHIDA, S. 1956 The pulsating viscous flow superposed on the steady laminar motion of incompressible fluids in a circular pipe. *Z. Angew. Math. Phys.* **7**, 403–422.

WOMERSLEY, J. R. 1955 Method for the calculation of velocity, rate of flow and viscous drag in arteries when the pressure gradient is known. *J. Physiol.* **127**, 553–563.